

AB-Stacked Multilayer Graphene Synthesized *via* Chemical Vapor Deposition: A Characterization by Hot Carrier Transport

Carlos Diaz-Pinto,^{†,‡,§} Debtanu De,^{†,‡,§} Viktor G. Hadjiev,[‡] and Haibing Peng^{†,‡,*}

[†]Department of Physics and [‡]The Texas Center for Superconductivity, University of Houston, Houston, Texas 77204, United States.

[§]These authors contributed equally to this work.

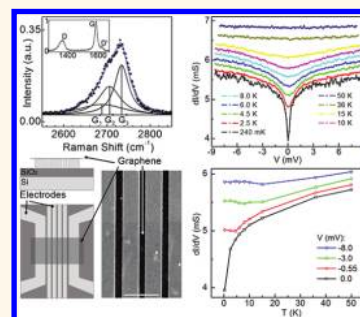
The synthesis of graphene on copper foils by chemical vapor deposition (CVD) has attracted considerable attention because of its potential in practical applications.^{1–6} The quality of CVD graphene³ has yet to match that of the graphene mechanically exfoliated from pristine graphite,^{7,8} and therefore, the CVD growth techniques are still under very active research. Various thermodynamic conditions involving both low pressure and ambient pressure are being addressed. In ref 9, the role of diffusion kinetics was discussed, and it was pointed out that at low pressure the synthesis process is self-limited with respect to the methane (which serves as the carbon source) flow rate, as opposed to the ambient pressure case. At ambient pressure, the mass transport of the carbon species to the catalyst surface dominates the synthesis process and produces multilayer graphene.⁹ However, for multilayer graphene, the CVD method usually leads to a turbostratic stacking order¹⁰ (*i.e.*, the layers are randomly oriented with respect to one another). To our knowledge, there has been no report on the CVD synthesis of continuous multilayer graphene films with AB-stacking order.¹¹ Recently, bilayer graphene with AB stacking has been achieved by CVD with low hydrogen flow rate or no hydrogen,^{12,13} and reduced hydrogen concentration has also led¹⁴ to the improvement of the quality of CVD graphene. It has been further realized¹⁵ that the absence of hydrogen can change the chemical kinetics of the decomposition of methane into active carbon and hydrogen. Therefore, the hydrogen concentration may play a role in determining the active carbon species at different stages of growth¹⁵ and

ABSTRACT We report the synthesis of AB-stacked multilayer graphene *via* ambient pressure chemical vapor deposition on Cu foils and demonstrate a method to construct suspended multilayer graphene devices. In four-terminal geometry, such devices were characterized by hot carrier transport at temperatures down to 240 mK and in magnetic fields up to 14 T. The differential conductance (dI/dV) shows a characteristic dip at longitudinal voltage bias $V = 0$ at low temperatures, indicating the presence of hot electron effect due to a weak electron–phonon coupling. Under magnetic fields, the magnitude of the dI/dV dip diminishes through the enhanced intra-Landau level cyclotron phonon scattering. Our results provide new perspectives in obtaining and understanding AB-stacked multilayer graphene, important for future graphene-based applications.

KEYWORDS: multilayer graphene · chemical vapor deposition · AB stacking · graphite · hot electron transport · nanostructure

hence may affect the growth rate, the quality, and the stacking order of multilayer graphene.

Here, the synthesis of AB-stacked multilayer graphene on Cu foils through ambient pressure CVD is demonstrated. We have achieved continuous multilayer graphene films with AB stacking by using a high methane flow rate and eliminating the hydrogen during the growth. This finding is important not only by shedding light on the CVD synthesis mechanism but also for offering controlled production of multilayer graphene with AB stacking by CVD. The multilayer graphene is further used to fabricate suspended multilayer graphene devices suitable for transport measurements. Hot electron transport is investigated through



* Address correspondence to haibingpeng@uh.edu.

Received for review September 28, 2011 and accepted January 27, 2012.

Published online January 27, 2012
10.1021/nn300326x

© 2012 American Chemical Society

a four-terminal configuration as a function of the measured longitudinal voltage drop V , temperature T , and magnetic field B . Such four-terminal transport results unambiguously demonstrate a distinct differential conductance dip at $V = 0$, an intrinsic transport behavior of multilayer graphene attributable to the presence of hot electron effect. We further observed that magnetic fields attenuate the hot electron effect and thus provide a way for its control by enhancing cyclotron phonon scattering.^{16,17}

RESULTS AND DISCUSSION

The growth of multilayer graphene was carried out on 25 μm thick Cu foils, using an ambient pressure methane CVD technique (see the Methods section for details of the CVD process). In brief, the graphene synthesis is realized in a key step with a mixture of a methane flow (13 mL/min) and an argon flow (150 mL/min) at a temperature of 1000 $^{\circ}\text{C}$ in a time period of ~ 10 min, while warming up is done under a pure hydrogen flow (200 mL/min) and cooling down is done under a pure Ar flow (150 mL/min). We find that increasing the methane flow (>10 mL/min) during the growth results in thicker multilayer graphene films, while a reduced methane flow (~ 1 mL/min) leads to single-layer graphene. In this study, we focus on devices made of multilayer graphene films ~ 3 nm (or ~ 9 layers) in thickness.

After CVD, thin flakes of multilayer graphene are obtained by etching away the underlying copper substrates with iron nitride solution. They are then transferred to a 200 nm SiO_2/Si substrate for Raman characterization. Figure 1a shows the Raman spectra (514 nm Ar^+ laser line) for a multilayer graphene sample. The most important feature observed in the Raman spectra is the asymmetry of the G' band at ~ 2730 cm^{-1} (with more weight in the higher frequency part), which is the signature of AB stacking in multilayer graphene.^{18–21} In contrast, for a multilayer graphene with a turbostratic stacking order, as typically reported in previous CVD work,¹⁰ the Raman spectra should have a symmetric G' band. The G' band can be fitted by three Lorentzian curves (Figure 1a, line) according to the methodology of ref 19. From the Raman intensity of the decomposed G'_2 and G'_3 bands (Figure 1a), $I_{G'_2}$ and $I_{G'_3}$, we find a c -axis crystalline coherence length $L_c = 10 + 10/(1.05 - A) \approx 29$ nm, where $A = I_{G'_2}/(I_{G'_2} + I_{G'_3})$. The estimated coherence length L_c is longer than the thickness of the multilayer graphene (~ 3 nm measured by an atomic force microscope), indicating single-crystal quality along the c -axis and supporting the observation of AB stacking from Raman measurements. The Raman spectra also reveal the presence of the disorder-induced bands D and D' at ~ 1364 and ~ 1626 cm^{-1} , respectively (Figure 1a, inset). From the relative intensity of the G band at ~ 1586 cm^{-1} to the D band, we can estimate

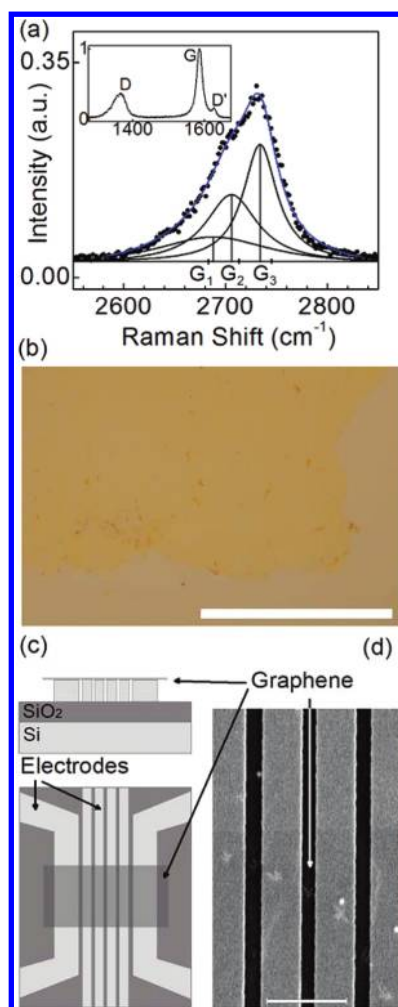


Figure 1. (a) Main panel: Raman G' band measured with a 514 nm laser (symbols) and the best fit to the data (solid line) for a CVD-grown multilayer graphene flake transferred onto a SiO_2/Si wafer. The curve of the best fit is decomposed into three Lorentzian peaks: G'_1 , G'_2 , and G'_3 centered at 2688, 2706, and 2734 cm^{-1} , respectively. Inset: Measured D, G, and D' bands. (b) Optical microscope image of a multilayer graphene sample transferred to a SiO_2/Si substrate with a 200 nm oxide layer. Scale bar: 1 mm. (c) Schematic cross section (top panel) and top view (bottom panel) of a multilayer graphene device (not to scale). The dark gray rectangle (bottom panel) on top of the predefined electrodes represents the multilayer graphene flake designed to be 44 μm in length and 30 μm in width. The metal electrodes are 60 nm thick (52.5 nm Pd on top of 7.5 nm Cr). The gap separating adjacent electrodes is ~ 400 nm wide. The width of the electrodes is ~ 1 μm for the four electrodes in the center and ~ 4 μm for the two at the edges. (d) Scanning electron microscope image of the device used in Figures 2–4. The multilayer graphene lying on top of the metal electrodes can be seen with a light contrast change (in the lower part of the image). Scale bar: 2 μm .

the in-plane crystallite size¹⁸ $L_a = 16.6(I_G/I_D) \sim 45$ nm for this sample. We stress that, in the CVD process, the elimination of hydrogen gas flow during the growth stage is critical for the synthesis of the AB-stacked multilayer graphene. To demonstrate the effect of the forming gas during growth, we performed controlled experiments for two CVD growth processes

with and without a hydrogen gas flow at 50 mL/min in addition to a methane flow at 13 mL/min during the growth stage and compared their Raman spectra (Figure S1 of the Supporting Information), which clearly demonstrates that the hydrogen gas flow leads to a symmetric G' peak (indicating turbostratic stacking) and a larger defect-induced D peak.

By using the etching and the transfer process, we are able to produce continuous multilayer graphene films in a size of a few millimeters, which is convenient for making devices for next-stage characterizations. Figure 1b presents an optical image of such a multilayer graphene film placed on a SiO_2/Si substrate. We have also performed Raman mapping experiments (Figure S2 of the Supporting Information) to further exam the uniformity of the films, which shows that the typical graphene film after etching and transferring to SiO_2/Si substrate is uniform in a scale of a few micrometers though it shows thickness variation in larger scale.

In order to characterize the electronic properties of such CVD-synthesized AB-stacking multilayer graphene, we further construct devices with a multilayer graphene flake suspended on top of six metal electrodes (see Methods section for device fabrication details). A schematic of the designed devices is shown in Figure 1c, along with a scanning electron microscope (SEM) image of a device partially covered by a suspended graphene flake (Figure 1d). The gap separating adjacent electrodes is ~ 400 nm wide, and the width of electrodes is ~ 1 μm . The available six electrodes allow multiple possible arrangements to be used in a four-terminal measurement, but in experiments, we select those four electrodes that have the lowest contact resistance to the graphene. The differential conductance dI/dV versus longitudinal voltage drop V is measured *via* a standard lock-in technique by supplying a DC current with a small AC modulation (503 Hz) through the outer I+ and I− electrodes and measuring both the DC and AC voltage drop between two inner V+ and V− electrodes. The dI/dV is also measured as a function of the gate voltage V_g with the degenerately doped silicon serving as a back gate (Figure 1c).

The dI/dV as a function of gate voltage V_g (Figure 2a) shows a maximum tuning of $\sim 50\%$ with respect to the minimum conductance point within a V_g range of ± 50 V at $T = 240$ mK, for a section of the multilayer graphene of Figure 1d.²² The minimum conductance point (neutral point) of the multilayer graphene is reached at a positive gate voltage $V_g = 24$ V, indicating a typical hole-doped (p-type) behavior which can be induced by the adsorption on the graphene surface.²³

The dependence of the dI/dV on the measured DC voltage V at $T = 240$ mK is shown in Figure 2b for fixed $V_g = 0$. The intriguing feature is a dip of dI/dV at $V = 0$ with a magnitude of $\sim 40\%$ of the zero bias dI/dV value. Previously, we also observed such a dip in suspended

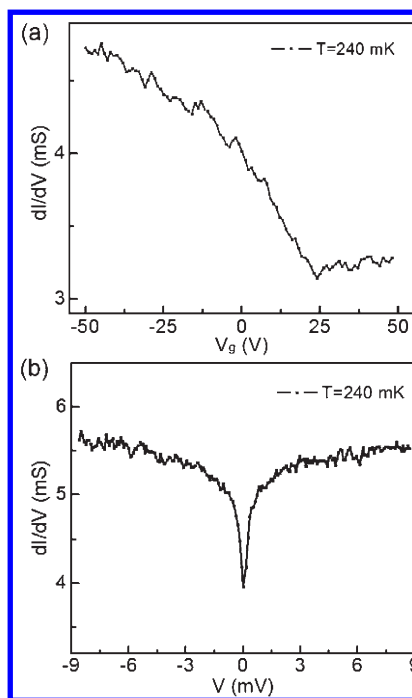


Figure 2. (a) Differential conductance dI/dV as a function of the gate voltage V_g at fixed longitudinal voltage bias $V = 0$. (b) Curve of dI/dV as a function of the measured longitudinal voltage bias V with $V_g = 0$. All data are taken at a temperature $T = 240$ mK.

graphitic multilayers by two-terminal transport measurements¹⁶ for which the role of the contact resistance had to be carefully considered. Here our four-terminal transport results unambiguously demonstrate that the observed dI/dV dip is an intrinsic transport behavior of multilayer graphene with no contribution from the contact barrier. As seen in our experiments (Figure S3 of the Supporting Information), the dI/dV dip remains at bias $V = 0$ regardless of the value of the gate voltage, thus ruling out its relation to graphene band features (*e.g.*, a neutral point), Coulomb blockade effect in an open quantum dot, Fabry–Perot resonance, or a possible presence of electron–hole puddles that partly form tunnel junctions.

Figure 3a presents the dI/dV versus V with $V_g = 0$ at various temperatures from 240 mK to 50 K (from bottom to top offset vertically for clarity). As the temperature is increased, the magnitude of the dI/dV dip is gradually suppressed and completely disappears for temperatures above $T = 8$ K. Figure 3b shows the dI/dV plotted as a function of temperature T for fixed V values. The temperature dependence of the dI/dV presents a similar behavior as the dI/dV versus V curve; that is, a dip of dI/dV is observed for $V = 0$ at low temperatures. This dip feature vanishes gradually as the bias V increases. The similar behavior of the dI/dV as a function of T and V suggests the presence of electron heating, and the dI/dV dip can be related to the hot electron effect^{16,24,25} as explained below. At finite bias,

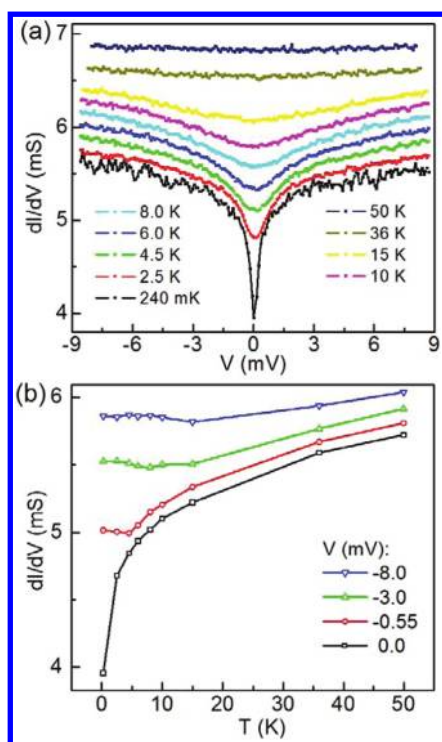


Figure 3. (a) Differential conductance dI/dV as a function of the measured longitudinal voltage bias V with $V_g = 0$ at different temperatures (from bottom to top: $T = 240$ mK, 2.5, 4.5, 6, 8, 10, 15, 36, and 50 K). For clarity, the curves are stacked by a vertical offset of 0.15 mS from bottom to top. (b) Data for dI/dV plotted as a function of temperature T for selected values of bias V . The curves are offset by 0.1 mS for clarity (from bottom to top: $V = 0$, -0.55 , -3.0 , and -8.0 mV).

the energy supplied to the charge carriers by the electric field cannot be transferred to the lattice fast enough due to a relatively weak electron–phonon scattering at low temperatures, resulting in an effective electron temperature T_e higher than the lattice temperature T_l (same as the cryostat temperature T in experiments). Therefore, the dI/dV value for a finite bias V measured at the cryostat temperature T should be equal to the dI/dV value for zero bias at an effective temperature T_e higher than T . Consequently, the experimentally obtained dI/dV versus V at a fixed low temperature ($T < 8$ K in Figure 3) should follow the trend of dI/dV versus T at zero bias ($V = 0$). This explains why the magnitude of the dip at zero bias in dI/dV versus V is suppressed as the temperature is increased (Figure 3a).¹⁶ At high enough temperatures ($T > 8$ K for the case of Figure 3), the achievable effective hot carrier temperature T_e is no longer higher than that of the lattice temperature due to enhanced electron–phonon scattering at high T , and therefore, the dI/dV dip disappears (Figure 3a).²⁶

In magnetic fields, the dI/dV as a function of V presents two notable changes (Figure 4). First, the overall dI/dV values drop with increasing magnetic fields (Figure 4a), indicating the presence of a strong positive magnetoresistance (MR) at high magnetic

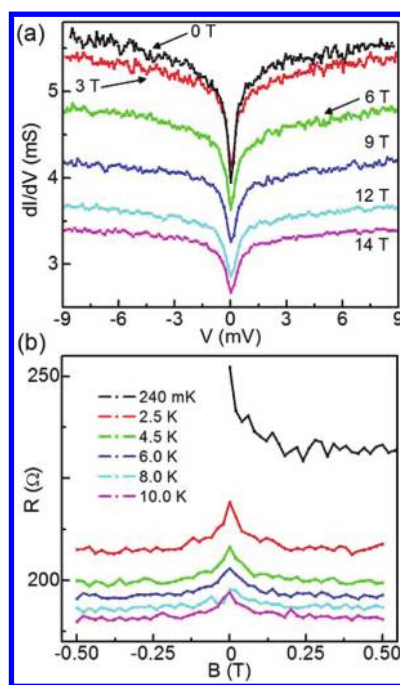


Figure 4. (a) Differential conductance dI/dV as a function of V with $V_g = 0$ V in different magnetic fields at a temperature 240 mK. The curves are plotted without any vertical offset. (b) Magnetoresistance data with fixed longitudinal bias $V = 0$ and gate voltage $V_g = 0$ at different temperatures. The weak localization effect is attenuated by increasing temperatures.

fields, which is commonly observed in bulk graphite^{27,28} or graphitic multilayers²⁹ and can be attributed to the interplay between long-range and short-range disorders.²⁹ At low magnetic fields (Figure 4b), negative magnetoresistance appears at low temperatures due to the weak localization effect, which indicates the influence of defects including grain boundaries in CVD-grown graphene.³⁰ Second, as the magnetic field is increased, there is an attenuation of the hot electron dip of dI/dV at $V = 0$ (Figure 4a), and this phenomenon is reproducibly observed in different samples (see Figure S4 of the Supporting Information). The magnitude of the dI/dV dip is considerably reduced at 14 T, as compared with the case at zero field. However, the persistence of the dI/dV dip even at 14 T suggests that weak localization is not the dominant source for the origin of the dI/dV dip in this sample. Otherwise, the dip should vanish at lower B fields.^{16,31} The B -field-induced suppression of the dI/dV dip observed here is more likely related to the enhanced electron–phonon scattering at high B fields,¹⁷ which diminishes the hot electron effect and thus the dI/dV dip. Under high magnetic fields, the intra-Landau level electron–phonon scattering is enhanced as a result of the increased degeneracy for a Landau level (equal to B/ϕ_0 with $\phi_0 = h/e$), making it easier for electrons to lose the energy gained from the electric field to the lattice. As a consequence, the effective electron temperature that can be reached at high magnetic fields is lower than

that achievable at zero field, leading to the attenuation of the hot electron dip near $V = 0$ (Figure 4a).

Moreover, we have observed similar gate tuning behavior, the persistence of the zero bias dI/dV dip, and its attenuation under magnetic fields for different sections of the multilayer graphene of Figure 1d (see Figure S4 of the Supporting Information), indicating the homogeneity of the electron transport properties in the as-prepared multilayer graphene.

CONCLUSION

We have succeeded in the synthesis of AB-stacked multilayer graphene *via* a distinct atmospheric pressure

CVD technique, as confirmed by Raman scattering experiments. Further investigation of its electronic properties is performed by the fabrication and electron transport studies of four-terminal multilayer graphene devices. The dI/dV as a function of longitudinal voltage bias V shows a dip pinned at $V = 0$,³² indicating the presence of hot electron effect due to a weak electron–phonon coupling. Under magnetic fields, the magnitude of the dI/dV dip diminishes through the enhanced intra-Landau level cyclotron phonon scattering. Our results provide new perspectives for obtaining and understanding AB-stacked multilayer graphene, important for future graphene-based applications.

METHODS

The CVD growth was carried out under ambient pressure in a 1 in. quartz tube furnace, using 25 μm thick copper foil (Alpha Aesar, item no. 13382). At room temperature, argon gas is used to flush the quartz tube at a rate of 2 L/min for at least 15 min. The Ar flow is then stopped; a hydrogen flow of 200 mL/min is started, and the temperature is raised to 1000 °C in ~ 18 min. With a subsequent waiting time of 20 min at 1000 °C, the H_2 flow is stopped, and an Ar flow of 150 mL/min is initialized and maintained for another 20 min. After that, a methane flow is established at 13 mL/min together with the Ar flow at 150 mL/min, followed by a waiting time of 10 min (typical target time for graphene growth). In the end, the CH_4 flow is turned off and the system is cooled to room temperature in ~ 1.5 h while keeping the Ar flow at 150 mL/min.

The following steps are needed for the fabrication of suspended multilayer devices after the CVD growth on copper foils. First, one side of the graphene-covered Cu foils is protected by spin coating of PMMA (~ 200 nm thick), while the graphene film on the other side of Cu foils is etched away using reactive ion etching with 50 sccm of O_2 at 50 W for 2 min. The obtained PMMA/graphene/copper foil is then cut into small ribbons ($\sim 2 \times 5$ mm) and placed in an $\text{Fe}(\text{NO}_3)_3$ aqueous etching solution (0.2 g/mL) for a few hours. After the copper is etched, the PMMA/graphene membrane is rinsed three times in deionized (DI) water, followed by a transfer to a SiO_2/Si substrate with a prepatterned array of electrode sets (Figure 1c). The sample is then blow dried with N_2 gas and kept in a vacuum desiccator overnight, and thus the membrane is strongly adhered to the substrate. Subsequently, the PMMA layer is removed by acetone at ~ 55 °C for 30 min. Finally, e-beam lithography and reactive ion etching are employed again to define a rectangular shape of the graphene suspended over electrodes (Figure 1c), followed by a lift-off process in acetone to remove the PMMA residue from the last lithography step. Measurements by atomic force microscope on typical devices show that the multilayer graphene sheets are suspended as designed (Figure S5 of the Supporting Information).

For the device of Figure 1d, we performed electrical measurements on the as-prepared sample without thermal annealing. Low-temperature measurements were carried out in a ^3He fridge at a base temperature of 240 mK. Magnetic fields are applied perpendicular to the multilayer graphene with a superconducting magnet inside a cryostat. The differential conductance dI/dV versus longitudinal voltage drop V is measured *via* a standard lock-in technique by supplying a DC current with a small AC modulation (503 Hz) through the outer I+ and I– electrodes and measuring both the DC and AC voltage drop between two inner V+ and V– electrodes. In the measurements for Figures 2–4, we used one AC current source with an internal resistance of 1 M Ω superimposed to a DC current source with an

internal resistance of 20 K Ω to obtain the differential conductance dI/dV as a function of V or V_g . We note that part of the AC current goes through the internal resistance of the DC current source so that the actual AC current dI through the graphene is smaller than the nominal value provided by the AC current source. For the device of Figures 2–4, the load resistance R_{load} is 1673 Ω , including circuit and contact resistance in series with the target graphene resistance (250 Ω at $V_g = 0$). The maximum variation of the graphene resistance as a function of V or V_g is no more than 100 Ω , much less than the internal resistance of both current sources. Thus the actual dI/dV can be obtained accurately by multiplying a scaling factor calculated based on the load resistance (our controlled experiments with a single current source to measure dI/dV versus V_g have confirmed this). All of the dI/dV values shown in this work are the accurate values after the correction.

The Raman measurements were done using a Horiba, JY Raman microscope equipped with a tunable Ar^+ laser set to operate at 514 nm in order to compare the measured spectra directly with those reported in literature, unless the laser wavelength is specified for certain experiments.

Conflict of Interest: The authors declare no competing financial interest.

Supporting Information Available: Additional experimental results are presented on the effect of hydrogen during the graphene growth, Raman mapping of a graphene film, the differential conductance dI/dV as a function of bias V with different fixed gate voltages V_g , electron transport data for different sections of the device under study in the main text, and the AFM image of a suspended multilayer graphene device. This material is available free of charge *via* the Internet at <http://pubs.acs.org>.

REFERENCES AND NOTES

- Li, X. S.; Cai, W. W.; An, J. H.; Kim, S.; Nah, J.; Yang, D. X.; Piner, R.; Velamakanni, A.; Jung, I.; Tutuc, E.; *et al.* Large-Area Synthesis of High-Quality and Uniform Graphene Films on Copper Foils. *Science* **2009**, *324*, 1312–1314.
- Aleman, B.; Regan, W.; Aloni, S.; Altoe, V.; Alem, N.; Geng, C. B.; Maserati, L.; Crommie, M.; Wang, F.; Zettl, A. Transfer-Free Batch Fabrication of Large-Area Suspended Graphene Membranes. *ACS Nano* **2010**, *4*, 4762–4768.
- Cao, H.; Yu, Q.; Jauregui, L. A.; Tian, J.; Wu, W.; Liu, Z.; Jalilian, R.; Benjamin, D. K.; Jiang, Z.; Bao, J.; *et al.* Electronic Transport in Chemical Vapor Deposited Graphene Synthesized on Cu: Quantum Hall Effect and Weak Localization. *Appl. Phys. Lett.* **2010**, *96*, 122106.
- Milaninia, K. M.; Baldo, M. A.; Reina, A.; Kong, J. All Graphene Electromechanical Switch Fabricated by Chemical Vapor Deposition. *Appl. Phys. Lett.* **2009**, *95*, 183105.

5. Huang, X.; Yin, Z.; Wu, S.; Qi, X.; He, Q.; Zhang, Q.; Yan, Q.; Boey, F.; Zhang, H. Graphene-Based Materials: Synthesis, Characterization, Properties, and Applications. *Small* **2011**, *7*, 1876–1902.
6. Sun, Z.; Yan, Z.; Yao, J.; Beitler, E.; Zhu, Y.; Tour, J. Growth of Graphene from Solid Carbon Sources. *Nature* **2010**, *468*, 549–552.
7. Bolotin, K. I.; Sikes, K. J.; Jiang, Z.; Klima, M.; Fudenberg, G.; Hone, J.; Kim, P.; Stormer, H. L. Ultrahigh Electron Mobility in Suspended Graphene. *Solid State Commun.* **2008**, *146*, 351–355.
8. Bao, W.; Zhao, Z.; Zhang, H.; Liu, G.; Kratz, P.; Jing, L.; Velasco, J.; Smirnov, D.; Lau, C. N. Magnetoconductance Oscillations and Evidence for Fractional Quantum Hall States in Suspended Bilayer and Trilayer Graphene. *Phys. Rev. Lett.* **2010**, *105*, 246601.
9. Bhaviripudi, S.; Jia, X.; Dresselhaus, M. S.; Kong, J. Role of Kinetic Factors in Chemical Vapor Deposition Synthesis of Uniform Large Area Graphene Using Copper Catalyst. *Nano Lett.* **2010**, *10*, 4128–4133.
10. Lenski, D. R.; Fuhrer, M. S. Raman and Optical Characterization of Multilayer Turbostratic Graphene Grown via Chemical Vapor Deposition. *J. Appl. Phys.* **2011**, *110*, 013720.
11. We have noticed that there was a recent report of synthesis of islands of multilayer graphene with AB stacking (ref 33).
12. Yan, K.; Peng, H.; Zhou, Y.; Li, H.; Liu, Z. Formation of Bilayer Bernal Graphene: Layer-by-Layer Epitaxy via Chemical Vapor Deposition. *Nano Lett.* **2011**, *11*, 1106–1110.
13. Lee, S.; Lee, K.; Zhong, Z. Wafer Scale Homogeneous Bilayer Graphene Films by Chemical Vapor Deposition. *Nano Lett.* **2010**, *10*, 4702–4707.
14. Gao, L.; Ren, W.; Zhao, J.; Ma, L. P.; Chen, Z.; Cheng, H. M. Efficient Growth of High-Quality Graphene Films on Cu Foils by Ambient Pressure Chemical Vapor Deposition. *Appl. Phys. Lett.* **2010**, *97*, 183109.
15. Zhang, W.; Wu, P.; Li, Z.; Yang, J. First-Principles Thermodynamics of Graphene Growth on Cu Surfaces. *J. Phys. Chem. C* **2011**, *115*, 17782.
16. Lee, S.; Wijesinghe, N.; Diaz-Pinto, C.; Peng, H. B. Hot Electron Transport in Suspended Multilayer Graphene. *Phys. Rev. B* **2010**, *82*, 045411.
17. Diaz-Pinto, C.; Lee, S.; Hadjiev, V.; Peng, H. B. Probing Phonon Emission via Hot Carrier Transport in Suspended Graphitic Multilayers. *Solid State Commun.* **2011**, *151*, 1645–1649.
18. Pimenta, M. A.; Dresselhaus, G.; Dresselhaus, M. S.; Cancado, L. G.; Jorio, A.; Saito, R. Studying Disorder in Graphite-Based Systems by Raman Spectroscopy. *Phys. Chem. Chem. Phys.* **2007**, *9*, 1276–1291.
19. Cançado, L. G.; Takai, K.; Enoki, T.; Endo, M.; Kim, Y. A.; Mizusaki, H.; Speziali, N. L.; Jorio, A.; Pimenta, M. A. Measuring the Degree of Stacking Order in Graphite by Raman Spectroscopy. *Carbon* **2008**, *46*, 272–275.
20. Malard, L. M.; Pimenta, M. A.; Dresselhaus, G.; Dresselhaus, M. S. Raman Spectroscopy in Graphene. *Phys. Rep.* **2009**, *473*, 51–87.
21. In ref 34, it was reported that an asymmetric G' peak should also appear in tri- and tetralayer graphene with ABC-stacking order. However, we note that for the ABC-stacking multilayer, the asymmetric G' peak reported therein shows more weight in the lower frequency part, in contrast to the G' spectra observed in our samples with more weight in the higher frequency part as reported for AB-stacked multilayers (ref 35). We can also rule out the possibility of a mixed stacking of turbostratic layers with AB-stacked layers for the nine-layer sample of Figure 1a by comparing the G' line shape with that reported in ref 36 since there is no sign of contribution from turbostratic layers to the relative weight at frequency $\sim 2700\text{ cm}^{-1}$.
22. In multilayer graphene, the charge carriers induced by a back gate voltage are screened within a few layers (with a typical screen length $\sim 0.4\text{ nm}$) (see ref 37), and thus the gate tuning of the conductance is reduced in multilayer graphene when a parallel conduction model is considered. For a device geometry with only the bottom layer contacting electrodes, electrons have to be transferred from the first bottom layer to upper layers in order for the upper layers to contribute to the conduction. In the case of diffusive transport in multilayer samples, scattering enhances the probability of electron transfer into upper layers. Therefore, it can still be treated by a parallel conduction model even with a bottom-contact geometry, but if there might exist certain cases with a weak electron transfer between layers, the parallel conduction model does not apply and the bottom-contact geometry may affect the gate tuning behavior significantly.
23. Novoselov, K. S.; Geim, A. K.; Morozov, S. V.; Jiang, D.; Zhang, Y.; Dubonos, S. V.; Grigorieva, I. V.; Firsov, A. A. Electric Field Effect in Atomically Thin Carbon Films. *Science* **2004**, *306*, 666–669.
24. Anderson, P. W.; Abrahams, E.; Ramakrishnan, T. V. Possible Explanation of Nonlinear Conductivity in Thin-Film Metal Wires. *Phys. Rev. Lett.* **1979**, *43*, 718–720.
25. Dolan, G. J.; Osheroff, D. D. Nonmetallic Conduction in Thin Metal Films at Low Temperatures. *Phys. Rev. Lett.* **1979**, *43*, 721–724.
26. We note that the Raman spectra indicate considerable defects in the CVD-produced multilayer graphene. However, even with defect scattering, hot electron effect can still be probed at finite bias if the electron–phonon coupling is relatively weak. We discuss here the role of different scattering mechanisms in the hot electron transport picture: (1) the electron–electron interaction leads to a thermal equilibrium within electrons themselves at an effective temperature T_e which is determined by the electron–phonon coupling strength; (2) the elastic scattering of carriers due to charged impurity atoms (defects) should not affect the hot electron temperature T_e ; (3) the inelastic scattering due to charged impurity atoms (defects) may affect the hot electron temperature if the relaxation of the resultant defect states is done via a phonon channel, or in other words leads to an enhanced effective electron–phonon coupling. Therefore, the defect scattering should not qualitatively change the hot electron transport, and the dI/dV dip is thus observable as long as the electron–phonon coupling is weak.
27. Spain, I. L. Galvanomagnetic Effects in Graphite. *Carbon* **1979**, *17*, 209–222.
28. Soule, D. E. Magnetic Field Dependence of the Hall Effect and Magnetoresistance in Graphite Single Crystals. *Phys. Rev.* **1958**, *112*, 698–707.
29. Diaz-Pinto, C.; Wang, X.; Lee, S.; Hadjiev, V.; De, D.; Chu, W. K.; Peng, H. B. Tunable Magnetoresistance in Suspended Graphitic Multilayers through Ion Implantation. *Phys. Rev. B* **2011**, *83*, 235410.
30. Jauregui, L. A.; Cao, H.; Wu, W.; Yu, Q.; Chen, Y. P. Electronic Properties of Grains and Grain Boundaries in Graphene Grown by Chemical Vapor Deposition. *Solid State Commun.* **2011**, *151*, 1100–1104.
31. Gorbachev, R. V.; Tikhonenko, F. V.; Mayorov, A. S.; Horsell, D. W.; Savchenko, A. K. Weak Localization in Bilayer Graphene. *Phys. Rev. Lett.* **2007**, *98*, 176805.
32. Our initial motivation to use suspended multilayer graphene is to minimize the electron–phonon scattering from the substrates. However, we have also observed the zero bias dI/dV dip in a sample with multilayer graphene lying on SiO_2/Si substrate and electrodes on top, indicating a hot electron effect due to a weak electron–phonon coupling even in nonsuspended multilayer graphene. This is reasonable since electron–phonon coupling has been reported to be weak even up to a temperature of $\sim 200\text{ K}$ for monolayer graphene lying on the SiO_2 substrate (see ref 38).
33. Robertson, A. W.; Warner, J. H. Hexagonal Single Crystal Domains of Few-Layer Graphene on Copper Foils. *Nano Lett.* **2011**, 1182–1189.

34. Lui, C. H.; Li, Z.; Chen, Z.; Klimov, P. V.; Brus, L. E.; Heinz, T. F. Imaging Stacking Order in Few-Layer Graphene. *Nano Lett.* **2011**, *11*, 164–169.
35. Ferrari, A. C.; Meyer, J. C.; Scardaci, V.; Casiraghi, C.; Lazzeri, M.; Mauri, F.; Piscanec, S.; Jiang, D.; Novoselov, K. S.; Roth, S.; Geim, A. K. Raman Spectrum of Graphene and Graphene Layers. *Phys. Rev. Lett.* **2006**, *97*, 187401.
36. Gupta, A.; Chen, G.; Joshi, P.; Tadigadapa, S.; Eklund, P. C. Raman Scattering From High-Frequency Phonons in Supported n-Graphene Layer Films. *Nano Lett.* **2006**, *6*, 2667–2673.
37. Visscher, P. R.; Falicov, L. M. Dielectric Screening in a Layered Electron Gas. *Phys. Rev. B* **1971**, *3*, 2541–2547.
38. Morozov, S. V.; Novoselov, K. S.; Katsnelson, M. I.; Schedin, F.; Elias, D. C.; Jaszczak, J. A.; Geim, A. K. Giant Intrinsic Carrier Mobilities in Graphene and Its Bilayer. *Phys. Rev. Lett.* **2008**, *100*, 016602.